Optimal Spatial Separation of High-Order Harmonics from Infrared Driving Lasers with an Annular Beam in the Overdriven Regime

Cheng Jin,[1,*] Xiangyu Tang,[1] Baochang Li,[1] Kan Wang,[1] and C. D. Lin[2]

[1] *Department of Applied Physics, Nanjing University of Science and Technology, Nanjing, Jiangsu 210094, China*
[2] *J. R. Macdonald Laboratory, Department of Physics, Kansas State University, Manhattan, Kansas 66506, USA*

(Received 1 March 2020; revised 4 May 2020; accepted 9 June 2020; published 20 July 2020)

We study high-order harmonic generation (HHG) with an annularly shaped high-power, high-repetition-rate laser. We investigate how the spatial separation (or divergence) of the incident laser and the generated high-order harmonics depends on the gas pressure when the laser intensity is in the overdriven regime. It is shown that, when the cone size of the incident annular beam is relatively large, the resulting harmonics are highly collimated along the propagation axis and are spatially separated from the incident beam. Under the overdriven condition, dynamic phase matching favors HHG emissions from short-trajectory electrons that are efficiently built up in the second half of the gas medium. We verify that using an annular beam is a simple and effective method for separating the intense incident infrared laser from the generated high harmonics. Such high-flux and low-divergence light pulses are expected to be powerful sources in the laboratory for ultrafast probing of electron dynamics.

DOI: 10.1103/PhysRevApplied.14.014057

I. INTRODUCTION

High-order harmonic generation (HHG) due to the nonlinear interaction between an intense femtosecond laser and a gas medium has become an important tool for providing attosecond light sources from the extreme ultraviolet (XUV) to water window soft x-rays [1–5] and keV region [6] for laboratory applications. With such light sources, a number of research topics and applications have been triggered, including attosecond science [7], HHG spectroscopy [8], nanoscale structure imaging [9], and assisted free-electron lasers [10], to name just a few. To become a useful light source, good beam quality of the harmonics is essential, which requires high photon flux and low divergence. Traditionally, the former can be accomplished either by improving phase-matching conditions in a nonlinear gas medium [11,12] or by synthesizing multicolor waveforms to enhance the harmonic yields from single emitters [13–16]. For achieving low divergence, one may adjust the macroscopic conditions in a gas-filled waveguide [17]. This issue has received some attention very recently [18]. It can be resolved by using a spatially chirped beam [19] or by using a two-color orthogonally polarized laser pulse [20]. In addition, low divergence can be measured with various techniques [19], for example, spectral wavefront optical reconstruction by diffraction [21].

An alternative approach to obtain high photon flux of HHG is to use high-power, high-repetition-rate lasers [22], such as fiber [23], slab [24], and thin-disk lasers [25]. These lasers can deliver a pulse energy of several hundreds of microjoules and a repetition rate of 10–100 kHz, with average power exceeding 1 kW. Such pulses are expected to greatly enhance the photon flux of high-order harmonics compared to the traditional Ti:sapphire lasers. On the other hand, for applications, the harmonic beam generated in the gas medium has to be spatially separated from the co-propagating infrared (IR) driving laser. For a low-average-power driving laser, a common method to block the residual IR pulse is to employ a thin metallic filter (hundreds of nanometers in thickness) [26–28], which can effectively transmit XUV radiation. However, this approach cannot be applied to high-average-power lasers where the generated heat can damage the filters.

To isolate high-order harmonics using high-power driving lasers, several optical techniques have been incorporated into the HHG setups [29], for instance, using diffraction gratings [30], grazing incidence plates [31], and microchannel plates [32], or by employing a noncollinear generation scheme [33,34]. All of these methods have certain limitations. Alternatively, one simple, efficient, and intrinsically stable method is to adopt an annular beam. This method was originally proposed by Peatross *et al.* in 1994 [35], and has been applied in HHG experiments recently by Klas *et al.* [36] and by Gaumnitz *et al.* [37]. In their experiments, using an annularly shaped beam, Klas *et al.* [36] reported that the HHG conversion efficiency

*cjin@njust.edu.cn

is reduced only by 27% when compared with that from a Gaussian beam under identical conditions. Meanwhile, Gaumnitz *et al*. [37] measured spatially resolved harmonic spectra reaching a cutoff energy of 90 eV with a few-cycle annular beam when the laser intensity is relatively low (approximately 5×10^{14} W/cm^2). They showed that divergence angles of harmonics are reduced compared with the full Gaussian beam.

From these experimental studies, it is revealed the potential of using annular beams for the generation of high-flux harmonics with high-power driving lasers. However, there are a number of questions remaining unresolved: (i) Does the cone size of an annular beam affect the spatial separation between the few-cycle IR laser and the HHG beam? (ii) Could such separation still be possible if the harmonic generation is optimized (for emission yield, cutoff energy, and divergence) in the overdriven intensity regime? (iii) What is the mechanism for the buildup of HHG using an annular beam? (iv) How does one compare the efficiency of harmonic generation of an annular beam with that of a Gaussian beam?

Our main goal in this work is to answer these questions through simulations. We systematically study the spatial separation of IR laser and high-harmonic beam by increasing gas pressure and changing the cone size of the annular beam. The phase-matching mechanism of obtaining high-flux and well-collimated HHG with an annular beam is carefully analyzed. We also check the spatial separation of longer-wavelength laser and HHG in the extended spectral region.

II. TYPICAL SETUP FOR GENERATING AN ANNULAR BEAM AND DETAILS OF SIMULATION

An annular laser beam whose center part is blank can be created either by inserting a block before focusing [35] or by using a perforated mirror with a central hole [36–38], as sketched in Fig. 1(a). In this work, the focusing mirror is set with a diameter of $d = 9$ mm and a focal length of $f = 500$ mm. The size (or diameter) of the laser block, defined with respect to the diameter of the focusing mirror, is μd, where $\mu < 1$. A Gaussian beam is incident into the laser block; its electric field is $E(\rho) = E_0 \exp[-(\rho/w_0)^2]$, where E_0 is the on-axis peak electric field and ρ is the radial coordinate. The beam waist is set at $w_0 = 4.5$ mm and the distance between the laser block and the focusing mirror is $h = 500$ mm. For a monochromatic Gaussian beam, one can obtain a pure annular beam in the far field if $\mu \neq 0$, as displayed in Fig. 1(a). If a gas jet is placed at the focus and the divergence of the HHG is small, then it can be well separated from the driving laser beam. Note that in this scheme the input laser energy is not fully used, but the pulse energy and the spectral range of the harmonics can be efficiently preserved.

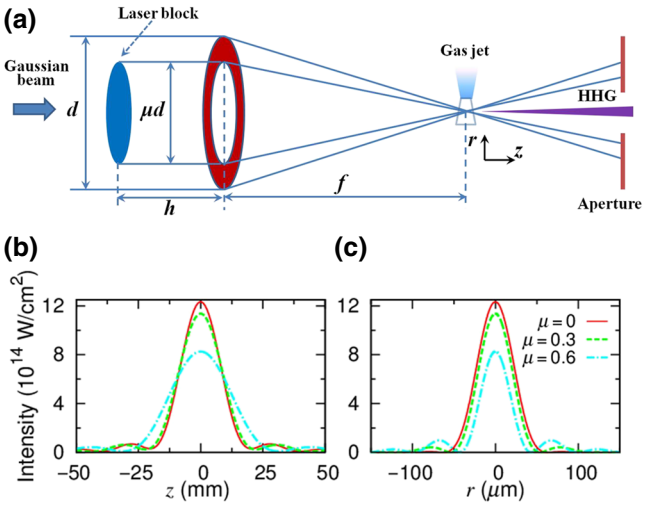

FIG. 1. (a) Schematic setup for producing an annular beam for generating high-order harmonics. The focusing mirror has a diameter d and a focal length f. The diameter of an optical block (or a hole in the mirror) is defined as μd. The distance between the block and focusing mirror is h. The input Gaussian beam has a beam waist $w_0 = d/2$, and the gas jet is put at the laser focus. When μ is properly chosen, the driving laser and high-harmonic field can be spatially separated in the far field. Laser intensity distribution (b) along the axial direction ($r = 0$) and (c) along the radial direction at the focal plane ($z = 0$) for different μ. The ratio of pulse energy for the input Gaussian beam is set as 1, 1.24, and 2.46 when $\mu = 0$, 0.3, and 0.6, respectively, such that the pulse energies going through the focusing mirror are the same. Laser wavelength is 800 nm.

For a fair comparison of HHG driven by different annular beams ($\mu \neq 0$) or a Gaussian beam ($\mu = 0$), we assume that the pulse energies going through the focusing mirror are the same. That means the pulse energies of input Gaussian beams are varied. Note that a similar comparison between an annular Bessel-Gauss beam and a Gaussian beam has been demonstrated in a pioneering work by Altucci *et al*. [39]. We use neon gas as the generating medium. With the goal of generating highest harmonic yields, the focusing laser intensity is chosen beyond the over-barrier intensity (approximately 8×10^{14} W/cm^2) [40]. Following the diffraction theory under the paraxial approximation, the electric field of the laser beam around the focus is [41]

$$E'(r,z) = \frac{ik}{B(z)} \int_{\mu d/2}^{d/2} E(\rho) J_0\left[\frac{kr\rho}{B(z)}\right] \times \exp\left[-ik\frac{Dr^2 + A(z)\rho^2}{2B(z)}\right] \rho d\rho, \quad (1)$$

where $k = 2\pi/\lambda_0$ and λ_0 is the central wavelength. For the optical system in Fig. 1(a), the ray matrix elements in

Eq. (1) are

$$\begin{aligned} A(z) &= -z/f\,, \\ B(z) &= z + f\, - zh/f\,, \\ C &= -1/f\,, \\ D &= 1 - h/f\,. \end{aligned} \tag{2}$$

Note that Eq. (1) is expressed in a reference frame moving at the speed of light, and element C is used in an alternative form of $E'(r,z)$ only when $B = 0$ in Eq. (2) [41]. For two annular beams and one Gaussian beam, the intensity distribution along the propagation axis is shown in Fig. 1(b). Meanwhile, Fig. 1(c) presents the intensity distribution along the radial direction at the focal plane. Here, we use a laser wavelength of 800 nm. The small outer peaks for $\mu = 0$ in Fig. 1(b) are due to the truncation of tail of the input Gaussian beam. Bessel-like beams can be identified for two annular beams with $\mu \neq 0$. The peak laser intensity is varied from 12.3×10^{14} to 8.2×10^{14} W/cm^2 when μ is increased from 0 to 0.6.

To simulate theoretical high-order harmonics that can be compared to experiment, one needs to take into account the single-atom response due to the interaction between an atom and the driving laser, and the macroscopic propagation of the fundamental laser and the high-harmonic field in the gaseous medium. The latter is obtained by solving three-dimensional Maxwell equations (see Ref. [42]). The single-atom response is computed by using the quantitative rescattering model [43–45]. The propagation of the driving laser and high-harmonic fields from the exit plane of the gas medium (near field) to a plane far away (far field) in the vacuum can be formulated in terms of Hankel transformation [42,46,47], which takes the same form as Eq. (1). In the simulation, we use a five-cycle laser pulse with a central wavelength of 800 nm (or 1200 nm). The pulse energy after the focusing mirror is about 480 μJ for the 800-nm laser. A 1-mm-long gas jet with uniform distribution is placed at the laser focus.

III. HIGH HARMONICS GENERATED BY 800-NM LASERS

A. Gas pressure dependence of harmonic spectra

To optimize harmonic yields in the overdriven regime, the gas pressure is varied. We show the simulated macroscopic HHG spectra of Ne atoms driven by 800-nm lasers for gas pressure from 50 to 500 Torr in Fig. 2. The harmonic yields are collected in the whole exit plane of the gas medium. For the three beams, one can see that with an increase of gas pressure, the harmonic yields in the plateau are progressively increased and the harmonic cutoff energy is gradually decreased. The best balance between the harmonic yield and plateau spectral range is reached at about 300 Torr, which is considered to be the optimal pressure.

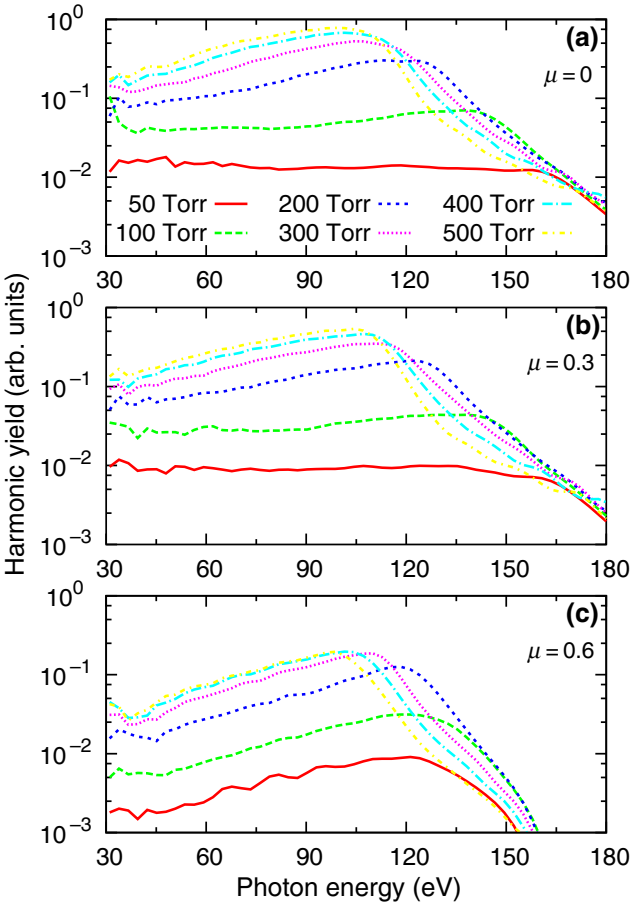

FIG. 2. Simulated HHG spectra generated with high-intensity 800-nm laser pulses versus gas pressure for different beam truncations defined by μ: (a) 0; (b) 0.3; (c) 0.6. The harmonic yields are integrated over the radial direction in the near field. Harmonic spectra are smoothed using Bezier curves for easy visualization. Optimal pressure for the best harmonic yields and best spectral region is found at 300 Torr for the three setups with different values of μ. See text for additional laser parameters.

For μ varying from 0 to 0.6, at the optimal pressure, the cutoff energy constantly appears at 110 eV, indicating that the driving lasers are saturated. The calculated conversion efficiency of high harmonics (integrated from 30 to 180 eV) is decreased from 1.9×10^{-5}, to 1.3×10^{-5}, to 6.2×10^{-6}. Note that in our previous study [48] using a standard Gaussian beam with a focusing intensity of about 10×10^{14} W/cm^2, we also found that the optimal pressure is 300 Torr. In the experiment of Gaumnitz *et al.* [37], the reported harmonic cutoff energy is very close to 110 eV when the full beam is used. One can see that harmonic yields in Fig. 2(c) grow with harmonic order at all pressures, while in Figs. 2(a) and 2(b) the harmonic yields are flat at low pressure, but grow at high pressure. Since for $\mu = 0$ and $\mu = 0.3$ the laser intensities are higher, bigger ionization in the higher-pressure regime incurs

large plasma dispersion, rendering peak laser intensity not reached as the laser propagates in the gas.

B. Spatial separation of the driving laser and high-harmonic beam

Next, we analyze the spatial separation of the driving laser and the high harmonics at the optimal pressure of 300 Torr. The spectral intensity distributions of the driving lasers versus the divergence angle are shown in Figs. 3(a), 3(c), and 3(e) after interacting with the Ne gas. For the driving laser the broad spectral distribution is due to the use of few-cycle pulses and the nonlinear plasma broadening in the medium. The lineouts of the fundamental 800-nm wavelength are shown in Fig. 4(a). For $\mu = 0$, the maximum intensity is on the axis. The maximum moves to an off-axis position when μ is increased to 0.3, but there is still a considerable portion of intensity on the axis. When μ is further increased to 0.6, the on-axis portion is greatly suppressed while the off-axis portion is enhanced. The normalization factors of the peak intensity distributions for the three frames are indicated in Figs. 3(a), 3(c), and 3(e).

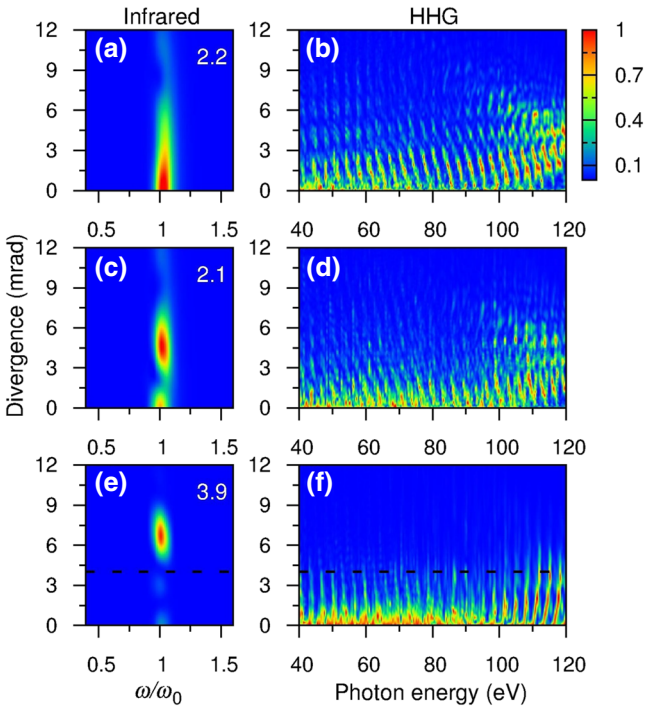

FIG. 3. Intensity distributions of the fundamental infrared laser and the generated high harmonics in the far field for different input beams. (a),(b) $\mu = 0$; (c),(d) $\mu = 0.3$; (e),(f) $\mu = 0.6$. In (a), (c), and (e), the laser intensities are normalized with respect to the maximum value (the normalization factors are labeled). ω_0 is the fundamental laser frequency. In (b), (d), and (f), the harmonic intensities are normalized at each photon energy. Full spatial separation of the IR laser and high-harmonic field is clearly demonstrated in (e),(f). Gas pressure is 300 Torr.

These results illustrate the shift of the driving laser to larger divergence of an annular beam.

The intensities of harmonic emissions in the far field versus the divergence and photon energy are presented in Figs. 3(b), 3(d), and 3(f). To examine the divergence properties of harmonics over such a broad spectral range, the intensity versus divergence for each photon energy is normalized independently. It is clearly seen that as μ is increased, the harmonics intensity moves toward the propagation axis, i.e., toward small divergence. This can be seen in Figs. 3(b), 3(d), and 3(f), or from the lineouts in Figs. 4(b)–4(d). The small residual pulse energy of the IR laser near the axis for $\mu = 0.6$ can be easily removed by adding a thin filter. It can also be eliminated by further increasing the size of the beam block (or μ). These results demonstrate that spatial separation of the IR driving laser and the generated high-order harmonics can be made possible by using an annular beam with a larger hole in the center while the divergence of HHG remains low. Note that similar spatial separation of harmonics and driving IR laser can also be achieved with other pulse energies by a proper macroscopic scaling [49–52].

C. Phase matching of efficient generation of collimated high harmonics

To understand the occurrence of spatial separation of the driving laser and the generated harmonics demonstrated in Fig. 3, we examine the phase matching by following the spatiotemporal evolution of the driving laser in the reference frame at three selected positions, one at the entrance, one at the middle, and one at the exit of the gas jet, as shown in Fig. 5. At the entrance, before interacting

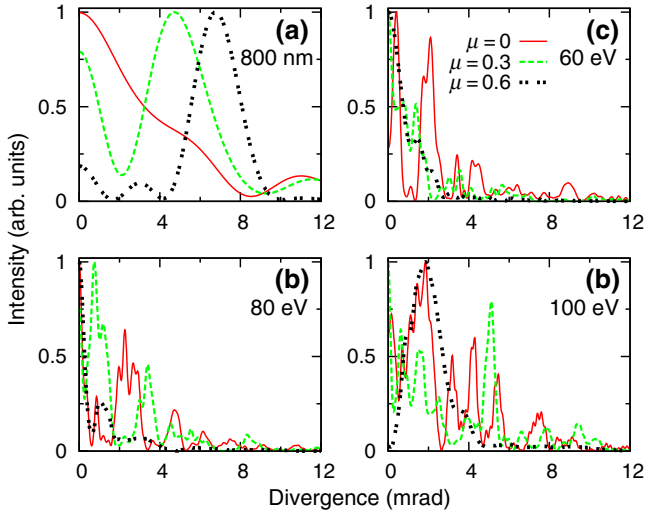

FIG. 4. Lineouts of intensity distributions of IR laser and high harmonics versus divergence in Fig. 3 for the fundamental laser (a) and for selected high harmonics (b)–(d).

with gas, the laser intensities have Gaussian profiles in time and Gaussian-like distributions in the radial direction, similar to those in Fig. 1(c). With an increase of propagation distance, the peak intensities decrease gradually. The spatiotemporal intensity distributions are greatly reshaped mostly due to plasma defocusing caused by excessive free electrons at the high ionization level. One can clearly see effective wavefront rotations [53,54] because the weaker intensity at larger radial distance remains the same while the higher intensity at smaller radial distance is reduced by the plasma defocusing, which is also accompanied by a blue shift in time mostly in the trailing edge of the beam. These effects become more prominent with higher input peak intensities [see Figs. 5(b), 5(c), 5(e), and 5(f)]. On the other hand, the intensity distributions are more spread when $\mu = 0.6$ even though the pulse energy through the focusing mirror is kept the same. Thus, the input peak intensity is smaller compared to that for $\mu = 0$ and 0.3 [see Fig. 5(g)] and less severe reshaping of the laser beam is displayed [see Figs. 5(h) and 5(i)]. The complicated evolution of spatiotemporal laser pulse inside a gas medium is responsible for the divergence behavior of high harmonics.

We next look at the time-frequency analysis of the resulting high harmonics exiting from the gas medium in Fig. 6. At small radial distances, only short-trajectory emissions are present. They are positive chirped for different μ. These emissions lead to small divergence of harmonics in the far field. At large radial distances, both short- and long-trajectory emissions appear due to wavefront rotations when $\mu = 0$ and 0.3. The long-trajectory emissions cause larger divergence in high harmonics in the far field, as seen in Figs. 3(b) and 3(d). For $\mu = 0.6$, short-trajectory emissions are still dominant at large radial distances [see Fig. 6(f)]. This explains why small-divergence harmonics over a broad spectral range can be generated in Fig. 3(f).

To further observe the effect of reshaping of the driving laser pulses on the harmonic generation process, we follow how harmonic fields are built up inside the gas medium. In Fig. 7, we can see the evolution of selected harmonics along z is oscillatory, at both small and large radial distances, for $\mu = 0$ and 0.3. Therefore, the coherence lengths for these harmonics are much smaller than the length of the gas medium, and the phase matching is poor. For $\mu = 0.6$, at $r = 10$ or 20 μm, the yields

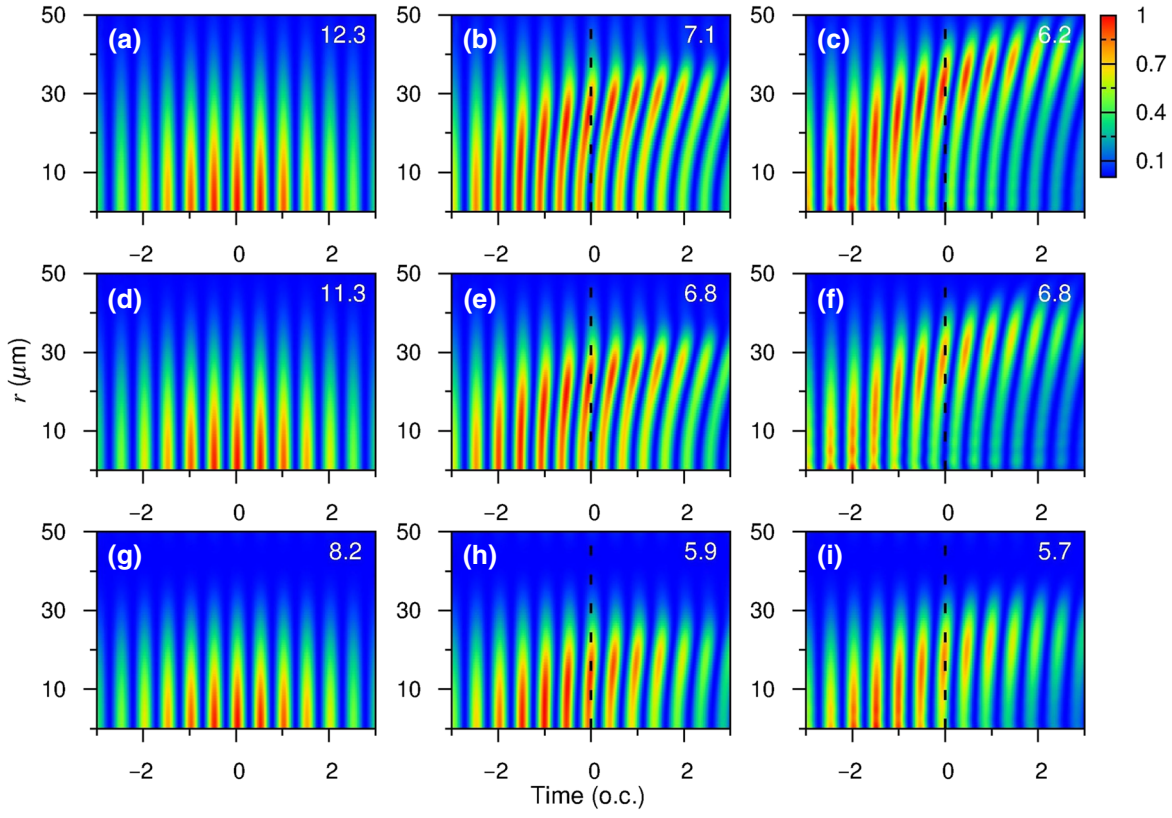

FIG. 5. Spatiotemporal laser intensity distributions of 800-nm lasers at the entrance (a),(d),(g), the middle (b),(e),(h), and the exit (c),(f),(i) of the gas medium for different input beams. From top to bottom, $\mu = 0$, 0.3, and 0.6, respectively. Laser intensities in each panel are normalized with respect to the maximum one (as labeled in units of 10^{14} W/cm^2). Here o.c. means the optical cycle of the 800-nm laser. Gas pressure is 300 Torr. Dashed lines are guides to the eye to see wavefront rotation of the laser pulses.

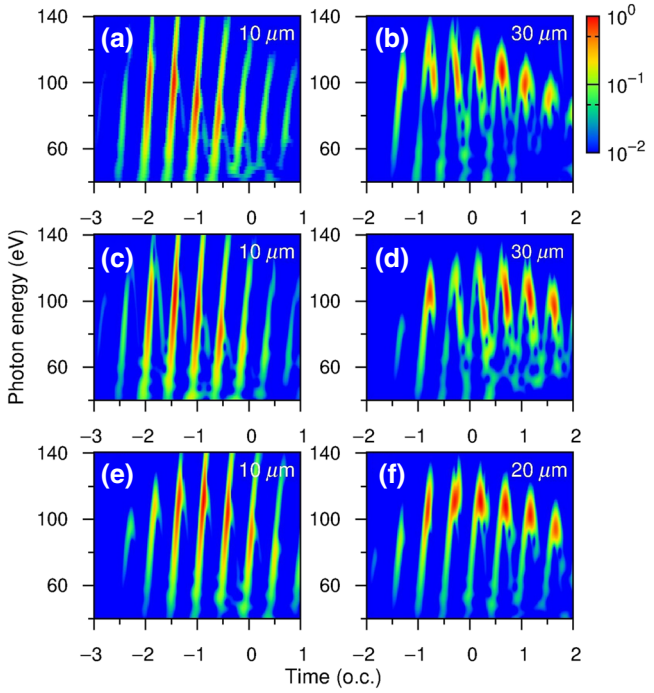

FIG. 6. Time-frequency analysis of harmonic emissions (normalized) for selected radial distances (as labeled) at the exit plane for different input beams. The size of the optical block changes from $\mu = 0$ (a),(b) to 0.3 (c),(d) to 0.6 (e),(f). Gas pressure is 300 Torr. The optical cycle (o.c.) is defined with respect to the fundamental 800-nm laser.

of harmonics are not efficiently accumulated in the first half of the gas medium (i.e., z is from -0.5 to 0 mm), but they increase monotonically in the second half [see Figs. 7(e) and 7(f)]. The coherence length of harmonics (the length between the positions of the minimum and the maximum yields) is about 0.5 mm (close to half the length of the gas medium). This also shows that good phase matching has been achieved for high harmonics over a broad spectral region in the second half of the gas medium.

Coherence length (or phase mismatch) can be calculated as in Refs. [55,56] if the driving laser pulse is not shaped. This is not the case for overdriven laser intensities here. Instead, coherence length of high harmonics can be obtained by calculating the phase mismatch [48]:

$$\Delta k \approx [(q-1)\omega_0 \Delta t - \alpha_i \Delta I]/\Delta z, \tag{3}$$

where q is the harmonic order and Δt and ΔI are the shift of the peak electric field in time and intensity variation over a propagation distance Δz, respectively. For short-trajectory harmonics in the plateau, $\alpha_i \approx 1 \times 10^{-14}$ rad cm^2/W, and this value is about 13.7×10^{-14} rad cm^2/W for cutoff harmonics. For $\mu = 0.6$, the electric waveforms of laser pulse at different z are plotted together in Fig. 8. From this figure, one can compare the

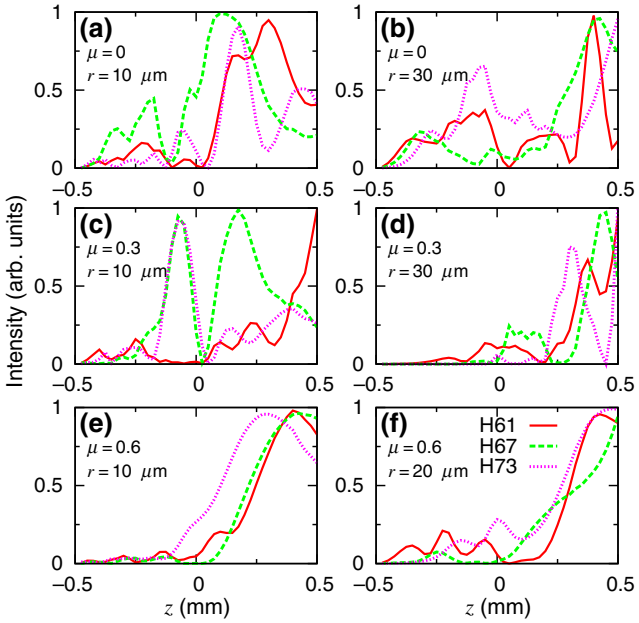

FIG. 7. Evolution of selected harmonics at different radial distances [$r = 10$ μm (a),(c),(e) and 30 μm (b),(d) and 20 μm (f)] with propagation distance z, for three input beams and harmonic orders as indicated. Gas pressure is 300 Torr.

field strength of $z = 0$ mm with that of $z = 0.5$ mm near the peak at -1.5 optical cycle (o.c.) if $r = 10$ μm or at -1.0 o.c. if $r = 20$ μm. Then ΔI over a propagation distance $\Delta z = 0.5$ mm can be obtained. Meanwhile, Δt can be extracted from the shift of the peak field position. Using Eq. (3), the values of calculated coherence length are shown in Table I. One can see the coherence length at $r = 10$ μm is slightly larger than that at $r = 20$ μm. Both values of coherence length and their changes at different radial positions are in agreement with the results in Figs. 7(e) and 7(f). Such a phase-matching mechanism is the same as that identified in Ref. [48] using a Gaussian beam. To obtain well-collimated harmonics in the far field,

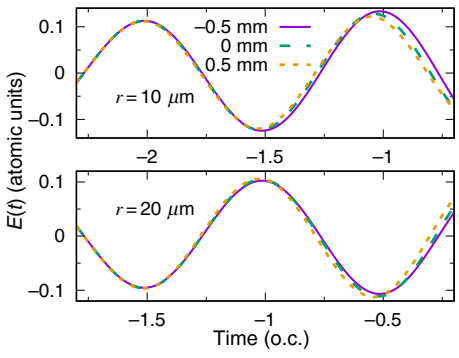

FIG. 8. The electric field of an 800-nm driving laser at different propagation distances for $\mu = 0.6$. Gas pressure is 300 Torr.

TABLE I. Harmonic coherence length at two radial positions for $\mu = 0.6$. Δt and ΔI between $z = 0$ and 0.5 mm are read from Fig. 8. $I_0 = 10^{14}$ W/cm^2. Coefficient α_i in Eq. (3) is chosen as 1×10^{-14} rad cm^2/W if $r = 10$ μm or 13.7×10^{-14} rad cm^2/W if $r = 20$ μm for selected high harmonics.

r (μm)	Δt (as)	ΔI (I_0)	$L_{coh} = \pi/\Delta k$ (mm)		
			H61	H67	H73
10	−20	−0.204	0.60	0.54	0.50
20	−22	0.092	0.36	0.34	0.32

dynamic phase matching due to reshaping of the driving laser pulse is desired [as shown in Figs. 7(e) and 7(f)]; also see Refs. [57,58]. These conditions can be reached only by setting the input laser intensity in the overdriven regime [see Figs. 5(g)–5(i)].

IV. SPATIAL SEPARATION WITH 1200-NM ANNULAR LASER BEAMS

In this section we take a look at how the driving laser and the generated harmonics are spatially separated using annular beams with wavelength at 1200 nm. For this wavelength, our prior experience [48] indicated that the pressure is 500 Torr for optimal harmonic yields. To maintain the same input laser intensities as for the 800-nm lasers, thus keeping the same overdriven conditions, the input pulse energy through the focusing mirror is taken as 1600 μJ.

The intensity distributions of the driving laser and the harmonics in the far field are shown in Fig. 9. For the mid-IR lasers, the longer wavelength makes the beams move away from the axis with larger divergence angles, as clearly seen in Fig. 9(e) for the case of $\mu = 0.6$. With the longer wavelength, the generated harmonic spectra extend to higher energy of 200 eV. The divergence of the harmonics, as shown in Fig. 9(f), is located very close to the axis. Thus at $\mu = 0.6$, the mid-IR lasers and the harmonics are well separated spatially. On the other hand, for $\mu = 0.3$ and the Gaussian beam, as shown in Figs. 9(a)–9(d), the mid-IR lasers and the harmonics cannot be spatially separated.

In Fig. 10, we show the spatiotemporal distributions of the driving laser intensities for the 1200-nm lasers at three positions (entrance, middle, and exit) of the gas jet. Comparing them with Fig. 5 for the case of 800-nm lasers, the laser fields along the radial direction are more spread out, but laser reshaping and wavefront rotation are identical to those seen in Fig. 5. This indicates that the same dynamic phase matching works for the generation of extremely well-collimated high harmonics in Fig. 9(f).

V. CONCLUSIONS

In this work, we have demonstrated that spatial separation of the driving laser and the generated harmonics in the far field can be achieved with an annular beam. Such a beam is created by inserting an optical block into the beam line before a focusing mirror. By using high pulse energy, the focused laser intensity can reach the overdriven regime. We show that the resulting high harmonics at the optimal pressure have small divergence. Substantial separation of the generated harmonics from the driving laser occurs only when the size of the optical block is large enough. We have analyzed the spatiotemporal laser field and the buildup of harmonic field along the propagation distance, and the time-frequency emission of the HHG at the exit plane of the gas medium. Such analysis reveals that dynamic phase matching is at work and harmonic emissions occur via recombination of short-trajectory electrons in the second half of the gas medium because of the slight reshaping and wavefront rotation of the driving laser. For the same pulse energy, using a Gaussian beam or an annular beam with a smaller optical block would not achieve considerable spatial separation and would result in large divergence of both infrared lasers and generated harmonics. These numerically illustrated results have validated the

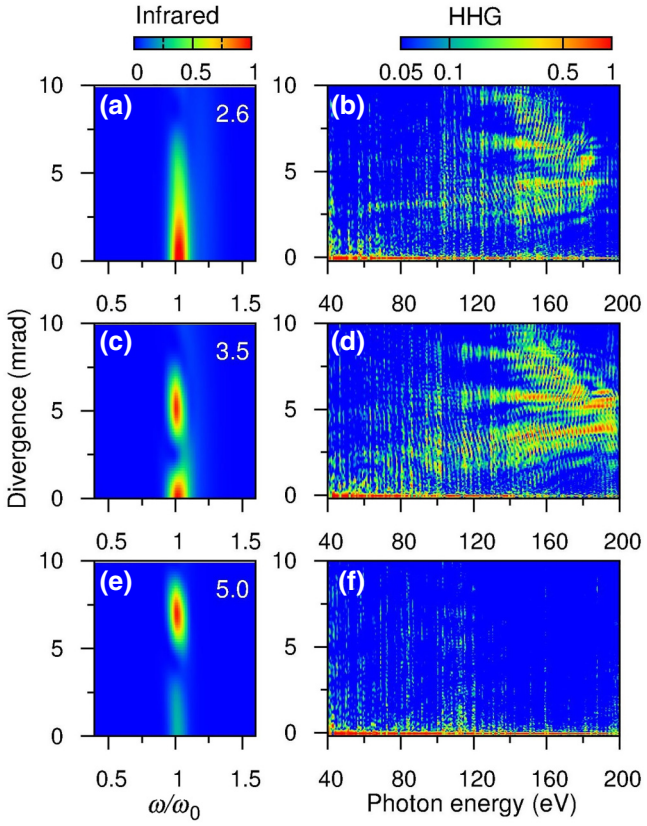

FIG. 9. Same as Fig. 3 except that the wavelength is 1200 nm and the gas pressure is 500 Torr. ω_0 and o.c. are both defined with respect to the 1200-nm laser. Note that laser intensities in (a), (c), and (e) are plotted in linear scale, while harmonic intensities in (b), (d), and (f) are in logarithmic scale.

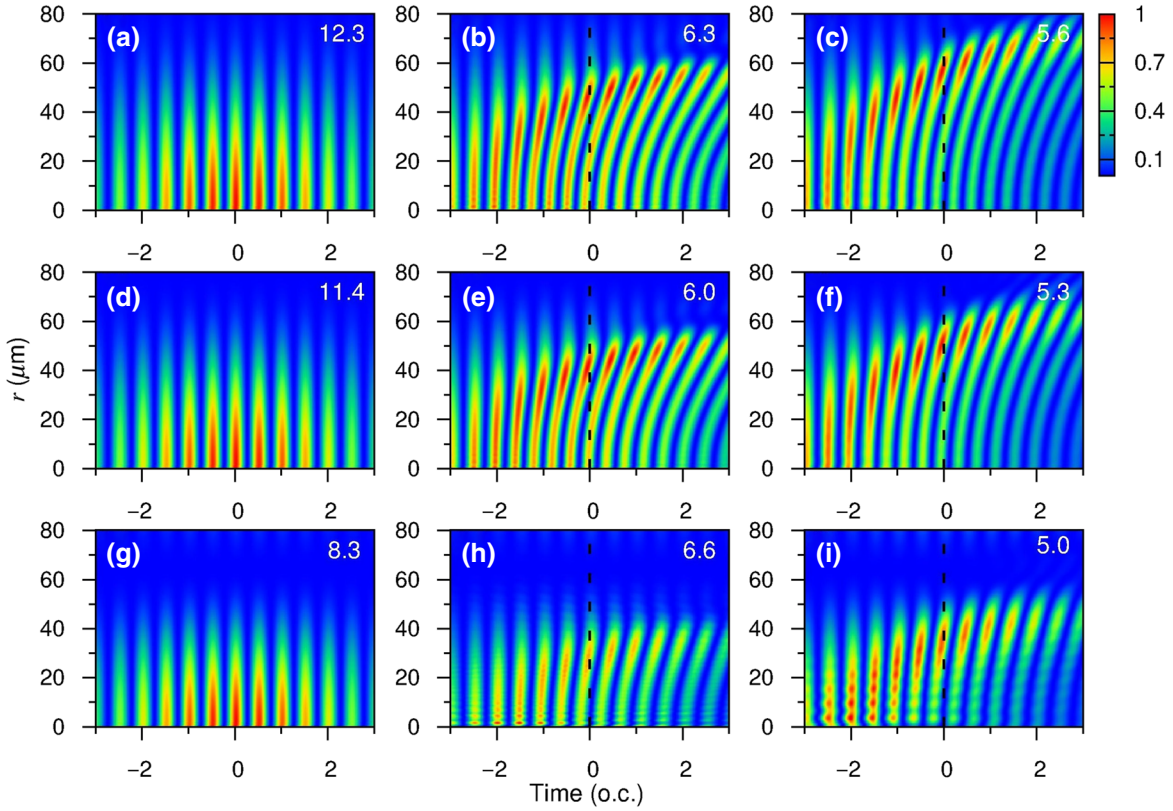

FIG. 10. Same as Fig. 5 but for 1200-nm lasers at 500 Torr.

essential nature of good phase matching for such overdriven pulses. We have shown that the same mechanism works for both 800- and 1200-nm annular beams. Other spatial beams, such as super-Gaussian or flat-top beams, may also be employed to generate high harmonics in this context.

With the development of laser technology, high-power and high-repetition-rate lasers are becoming available even for longer-wavelength mid-IR lasers [5,59–62]. Such lasers are likely to become new workhorses for generating high-flux, high-energy photons that can be used for spectroscopy, or as attosecond pulses for probing dynamics of electrons in atoms, molecules, and materials. With an annular beam it is possible to separate the incident beam from the generated harmonics. We expect that this study will help guide experimentalists in the realization of useful tabletop light sources from the XUV to x-rays.

ACKNOWLEDGMENTS

C.J., X.T., B.L., and K.W. are supported by National Natural Science Foundation of China (NSFC) under Grants No. 11774175, No. 91950102, and No. 11834004. C.D.L. is supported by Chemical Sciences, Geosciences, and Biosciences Division, Office of Basic Energy Sciences, Office of Science, U.S. Department of Energy under Grant No. DE-FG02-86ER13491.

[1] C. Spielmann, N. H. Burnett, S. Sartania, R. Koppitsch, M. Schnürer, C. Kan, M. Lenzner, P. Wobrauschek, and F. Krausz, Generation of coherent X-rays in the water window using 5-femtosecond laser pulses, Science **278**, 661 (1997).

[2] E. J. Takahashi, T. Kanai, K. L. Ishikawa, Y. Nabekawa, and K. Midorikawa, Coherent Water Window X Ray by Phase-Matched High-Order Harmonic Generation in Neutral Media, Phys. Rev. Lett. **101**, 253901 (2008).

[3] H. Xiong, H. Xu, Y. Fu, J. Yao, B. Zeng, W. Chu, Y. Cheng, Z. Xu, E. J. Takahashi, K. Midorikawa, X. Liu, and J. Chen, Generation of a coherent x ray in the water window region at 1 kHz repetition rate using a mid-infrared pump source, Opt. Lett. **34**, 1747 (2009).

[4] X. Ren, J. Li, Y. Yin, K. Zhao, A. Chew, Y. Wang, S. Hu, Y. Cheng, E. Cunningham, Y. Wu, M. Chini, and Z. Chang, Attosecond light sources in the water window, J. Opt. **20**, 023001 (2018).

[5] J. Pupeikis, P.-A. Chevreuil, N. Bigler, L. Gallmann, C. R. Phillips, and U. Keller, Water window soft x-ray source enabled by a 25 W few-cycle 2.2 μm OPCPA at 100 kHz, Optica **7**, 168 (2020).

[6] T. Popmintchev, M.-C. Chen, D. Popmintchev, P. Arpin, S. Brown, S. Ališauskas, G. Andriukaitis, T. Balciunas, O. D. Mücke, A. Pugzlys, A. Baltuška, B. Shim, S. E. Schrauth, A. Gaeta, C. Hernández-García, L. Plaja, A. Becker, A. Jaron-Becker, M. M. Murnane, and H. C. Kapteyn, Bright coherent ultrahigh harmonics in the keV X-ray regime

from mid-infrared femtosecond lasers, Science **336**, 1287 (2012).
[7] F. Krausz and M. Ivanov, Attosecond physics, Rev. Mod. Phys. **81**, 163 (2009).
[8] Y. Pertot, C. Schmidt, M. Matthews, A. Chauvet, M. Huppert, V. Svoboda, A. von Conta, A. Tehlar, D. Baykusheva, J.-P. Wolf, and H. J. Wörner, Time-resolved x-ray absorption spectroscopy with a water window high-harmonic source, Science **355**, 264 (2017).
[9] J. Miao, T. Ishikawa, I. K. Robinson, and M. M. Murnane, Beyond crystallography: Diffractive imaging using coherent x-ray light sources, Science **348**, 530 (2015).
[10] G. Lambert, T. Hara, D. Garzella, T. Tanikawa, M. Labat, B. Carre, H. Kitamura, T. Shintake, M. Bougeard, S. Inoue, Y. Tanaka, P. Salieres, H. Merdji, O. Chubar, O. Gobert, K. Tahara, and M.-E. Couprie, Injection of harmonics generated in gas in a free-electron laser providing intense and coherent extreme-ultraviolet light, Nat. Phys. **4**, 296 (2008).
[11] V. S. Yakovlev, M. Ivanov, and F. Krausz, Enhanced phase-matching for generation of soft X-ray harmonics and attosecond pulses in atomic gases, Opt. Express **15**, 15351 (2007).
[12] M. B. Gaarde, J. L. Tate, and K. J. Schafer, Macroscopic aspects of attosecond pulse generation, J. Phys. B: At. Mol. Opt. Phys. **41**, 132001 (2008).
[13] L. E. Chipperfield, J. S. Robinson, J. W. G. Tisch, and J. P. Marangos, Ideal Waveform to Generate the Maximum Possible Electron Recollision Energy for Any Given Oscillation Period, Phys. Rev. Lett. **102**, 063003 (2009).
[14] E. J. Takahashi, P. Lan, O. D. Mücke, Y. Nabekawa, and K. Midorikawa, Attosecond nonlinear optics using gigawatt-scale isolated attosecond pulses, Nat. Commun. **4**, 2691 (2013).
[15] S. Haessler, T. Balčiunas, G. Fan, G. Andriukaitis, A. Pugžlys, A. Baltuška, T. Witting, R. Squibb, A. Zaïr, J. W. G. Tisch, J. P. Marangos, and L. E. Chipperfield, Optimization of Quantum Trajectories Driven by Strong-Field Waveforms, Phys. Rev. X **4**, 021028 (2014).
[16] C. Jin, G. Wang, H. Wei, A.-T. Le, and C. D. Lin, Waveforms for optimal sub-keV high-order harmonics with synthesized two- or three-colour laser fields, Nat. Commun. **5**, 4003 (2014).
[17] C. Jin, G. J. Stein, K.-H. Hong, and C. D. Lin, Generation of Bright, Spatially Coherent Soft X-Ray High Harmonics in a Hollow Waveguide Using Two-Color Synthesized Laser Pulses, Phys. Rev. Lett. **115**, 043901 (2015).
[18] H. Wikmark, C. Guo, J. Vogelsang, P. W. Smorenburg, H. Coudert-Alteirac, J. Lahl, J. Peschel, P. Rudawski, H. Dacasa, S. Carlström, S. Maclot, M. B. Gaarde, P. Johnsson, C. L. Arnold, and A. L'Huillier, Spatiotemporal coupling of attosecond pulses, Proc. Natl. Acad. Sci. USA **116**, 4779 (2019).
[19] L. Quintard, V. Strelkov, J. Vabek, O. Hort, A. Dubrouil, D. Descamps, F. Burgy, C. Péjot, E. Mével, F. Catoire, and E. Constant, Optics-less focusing of XUV high-order harmonics, Sci. Adv. **5**, eaau7175 (2019).
[20] S. R. Abbing, F. Campi, F. S. Sajjadian, N. Lin, P. Smorenburg, and P. M. Kraus, Divergence Control of High-Harmonic Generation, Phys. Rev. Appl. **13**, 054029 (2020).
[21] E. Frumker, G. G. Paulus, H. Niikura, A. Naumov, D. M. Villeneuve, and P. B. Corkum, Order-dependent structure of high harmonic wavefronts, Opt. Express **20**, 13870 (2012).
[22] S. Hüdrich, J. Rothhardt, M. Krebs, S. Krebs, A. Klenke, A. Tünnermann, and J. Limpert, Single-pass high harmonic generation at high repetition rate and photon flux, J. Phys. B: At. Mol. Opt. Phys. **49**, 172002 (2016).
[23] M. Müller, M. Kienel, A. Klenke, T. Gottschall, E. Shestaev, M. Plötner, J. Limpert, and A. Tünnermann, 1 kW 1 mJ eight-channel ultrafast fiber laser, Opt. Lett. **41**, 3439 (2016).
[24] P. Russbueldt, T. Mans, J. Weitenberg, H. D. Hoffmann, and R. Poprawe, Compact diode-pumped 1.1 kW Yb:YAG Innoslab femtosecond amplifier, Opt. Lett. **35**, 4169 (2010).
[25] J.-P. Negel, A. Loescher, A. Voss, D. Bauer, D. Sutter, A. Killi, M. A. Ahmed, and T. Graf, Ultrafast thin-disk multipass laser amplifier delivering 1.4 kW (4.7 mJ, 1030 nm) average power converted to 820 W at 515 nm and 234 W at 343 nm, Opt. Express **23**, 21064 (2015).
[26] M. Hentschel, R. Kienberger, C. Spielmann, G. A. Reider, N. Milosevic, T. Brabec, P. Corkum, U. Heinzmann, M. Drescher, and F. Krausz, Attosecond metrology, Nature **414**, 509 (2001).
[27] R. Kienberger, E. Goulielmakis, M. Uiberacker, A. Baltuska, V. Yakovlev, F. Bammer, A. Scrinzi, T. Westerwalbesloh, U. Kleineberg, U. Heinzmann, M. Drescher, and F. Krausz, Atomic transient recorder, Nature **427**, 817 (2004).
[28] J. Itatani, J. Levesque, D. Zeidler, H. Niikura, H. Pépin, J. C. Kieffer, P. B. Corkum, and D. M. Villeneuve, Tomographic imaging of molecular orbitals, Nature **432**, 867 (2004).
[29] J. Rothhardt, G. K. Tadesse, W. Eschen, and J. Limpert, Table-top nanoscale coherent imaging with XUV light, J. Opt. **20**, 113001 (2018).
[30] A. K. Mills, T. J. Hammond, M. H. C. Lam, and D. J. Jones, XUV frequency combs via femtosecond enhancement cavities, J. Phys. B: At. Mol. Opt. Phys. **45**, 142001 (2012).
[31] O. Pronin, V. Pervak, E. Fill, J. Rauschenberger, F. Krausz, and A. Apolonski, Ultrabroadband efficient intracavity XUV output coupler, Opt. Express **19**, 10232 (2011).
[32] Q. Zhang, K. Zhao, J. Li, M. Chini, Y. Cheng, Y. Wu, E. Cunningham, and Z. Chang, Suppression of driving laser in high harmonic generation with a microchannel plate, Opt. Lett. **39**, 3670 (2014).
[33] S. Fomichev, P. Breger, B. Carre, P. Agostini, and D. F. Zaretsky, Non-collinear high-harmonic generation, Laser Phys. **12**, 383 (2002).
[34] D. D. Hickstein, F. J. Dollar, P. Grychtol, J. L. Ellis, R. Knut, C. Hernández-García, D. Zusin, C. Gentry, *et al.*, Non-collinear generation of angularly isolated circularly polarized high harmonics, Nat. Photon. **9**, 743 (2015).
[35] J. Peatross, J. L. Chaloupka, and D. D. Meyerhofer, High-order harmonic generation with an annular laser beam, Opt. Lett. **19**, 942 (1994).
[36] R. Klas, A. Kirsche, M. Tschernajew, J. Rothhardt, and J. Limpert, Annular beam driven high harmonic generation for high flux coherent XUV and soft X-ray radiation, Opt. Express **26**, 19318 (2018).

[37] T. Gaumnitz, A. Jain, and H. J. Wörner, Extreme-ultraviolet high-order harmonic generation from few-cycle annular beams, Opt. Lett. **43**, 4506 (2018).
[38] F. Schlaepfer, A. Ludwig, M. Lucchini, L. Kasmi, M. Volkov, L. Gallmann, and U. Keller, Gouy phase shift for annular beam profiles in attosecond experiments, Opt. Express **25**, 3646 (2017).
[39] C. Altucci, R. Bruzzese, D. D'Antuoni, C. de Lisio, and S. Solimeno, Harmonic generation in gases by use of Bessel-Gauss laser beams, J. Opt. Soc. Am. B **17**, 34 (2000).
[40] X. M. Tong and C. D. Lin, Empirical formula for static field ionization rates of atoms and molecules by lasers in the barrier-suppression regime, J. Phys. B: At. Mol. Opt. Phys. **38**, 2593 (2005).
[41] C. Jin and C. D. Lin, Comparison of high-order harmonic generation of Ar using truncated Bessel and Gaussian beams, Phys. Rev. A **85**, 033423 (2012).
[42] C. Jin, A. T. Le, and C. D. Lin, Medium propagation effects in high-order harmonic generation of Ar and N_2, Phys. Rev. A **83**, 023411 (2011).
[43] A. T. Le, R. R. Lucchese, S. Tonzani, T. Morishita, and C. D. Lin, Quantitative rescattering theory for high-order harmonic generation from molecules, Phys. Rev. A **80**, 013401 (2009).
[44] C. D. Lin, A. T. Le, C. Jin, and H. Wei, Elements of the quantitative rescattering theory, J. Phys. B: At. Mol. Opt. Phys. **51**, 104001 (2018).
[45] C. D. Lin, A. T. Le, C. Jin, and H. Wei, *Attosecond and Strong-Field Physics: Principles and Applications* (Cambridge University Press, Cambridge, 2018), p. 209.
[46] A. L'Huillier, Ph. Balcou, S. Candel, K. J. Schafer, and K. C. Kulander, Calculations of high-order harmonic-generation processes in xenon at 1064 nm, Phys. Rev. A **46**, 2778 (1992).
[47] V. Tosa, K. T. Kim, and C. H. Nam, Macroscopic generation of attosecond-pulse trains in strongly ionized media, Phys. Rev. A **79**, 043828 (2009).
[48] C. Jin and C. D. Lin, Spatially coherent high-order harmonics generated at optimal high gas pressure with high-intensity one- or two-color laser pulses, Phys. Rev. A **94**, 043804 (2016).
[49] J. Rothhardt, M. Krebs, S. Härich, S. Demmler, J. Limpert, and A. Tünermann, Absorption-limited and phase-matched high harmonic generation in the tight focusing regime, New J. Phys. **16**, 033022 (2014).
[50] C. M. Heyl, H. Coudert-Alteirac, M. Miranda, M. Louisy, K. Kovacs, V. Tosa, E. Balogh, K. Varjú, A. L'Huillier, A. Couairon, and C. L. Arnold, Scale-invariant nonlinear optics in gases, Optica **3**, 75 (2016).
[51] C. M. Heyl, C. L. Arnold, A. Couairon, and A. L'Huillier, Introduction to macroscopic power scaling principles for high-order harmonic generation, J. Phys. B: At. Mol. Opt. Phys. **50**, 013001 (2017).
[52] C. Jin and C. D. Lin, Control of soft X-ray high harmonic spectrum by using two-color laser pulses, Photonics Res. **6**, 434 (2018).
[53] V. Tosa, J. S. Lee, H. T. Kim, and C. H. Nam, Attosecond pulses generated by the lighthouse effect in Ar gas, Phys. Rev. A **91**, 051801(R) (2015).
[54] K. Kovács, M. Negro, C. Vozzi, S. Stagira, and V. Tosa, Attosecond lighthouse above 100 eV from high-harmonic generation of mid-infrared pulses, J. Opt. **19**, 104003 (2017).
[55] Ph. Balcou, P. Salières, A. L'Huillier, and M. Lewenstein, Generalized phase-matching conditions for high harmonics: The role of field-gradient forces, Phys. Rev. A **55**, 3204 (1997).
[56] C. Altucci, R. Bruzzese, C. de Lisio, M. Nisoli, E. Priori, S. Stagira, M. Pascolini, L. Poletto, P. Villoresi, V. Tosa, and K. Midorikawa, Phase-matching analysis of high-order harmonics generated by truncated Bessel beams in the sub-10-fs regime, Phys. Rev. A **68**, 033806 (2003).
[57] C. Jin, M.-C. Chen, H.-W. Sun, and C. D. Lin, Extension of water-window harmonic cutoff by laser defocusing-assisted phase matching, Opt. Lett. **43**, 4433 (2018).
[58] A. S. Johnson, D. R. Austin, D. A. Wood, C. Brahms, A. Gregory, K. B. Holzner, S. Jarosch, E. W. Larsen, S. Parker, C. S. Strüber, P. Ye, J. W. G. Tisch, and J. P. Marangos, High-flux soft x-ray harmonic generation from ionization-shaped few-cycle laser pulses, Sci. Adv. **4**, eaar3761 (2018).
[59] N. Thiré, R. Maksimenka, B. Kiss, C. Ferchaud, G. Gitzinger, T. Pinoteau, H. Jousselin, S. Jarosch, P. Bizouard, V. Di Pietro, E. Cormier, K. Osvay, and N. Forget, Highly stable, 15 W, few-cycle, 65 mrad CEP-noise mid-IR OPCPA for statistical physics, Opt. Express **26**, 26907 (2018).
[60] M. Neuhaus, H. Fuest, M. Seeger, J. Schötz, M. Trubetskov, P. Russbueldt, H. D. Hoffmann, E. Riedle, Z. Major, V. Pervak, M. F. Kling, and P. Wnuk, 10 W CEP-stable few-cycle source at 2 μm with 100 kHz repetition rate, Opt. Express **26**, 16074 (2018).
[61] U. Elu, M. Baudisch, H. Pires, F. Tani, M. H. Frosz, F. Köttig, A. Ermolov, P. St. J. Russell, and J. Biegert, High average power and single-cycle pulses from a mid-IR optical parametric chirped pulse amplifier, Optica **4**, 1024 (2017).
[62] M. Mero, Z. Heiner, V. Petrov, H. Rottke, F. Branchi, G. M. Thomas, and M. J. J. Vrakking, 43 W, 1.55 μm and 12.5 W, 3.1 μm dual-beam, sub-10 cycle, 100 kHz optical parametric chirped pulse amplifier, Opt. Lett. **43**, 5246 (2018).